RSC Advances

PAPER

View Article Online
View Journal | View Issue

Cite this: RSC Adv., 2025, 15, 30387

Theoretical prediction of a novel 2D TiOBr monolayer with negative Poisson's ratio using first-principles calculations

Shuzhen Li,†[a] Huabin Gong,†[a] Xiaobiao Liu[b] and Bo Yang*[a]

Received 1st July 2025
Accepted 12th August 2025

DOI: 10.1039/d5ra04655f

rsc.li/rsc-advances

Two-dimensional (2D) materials with novel mechanical behaviors and electronic characteristics have attracted extensive attention in multiple cutting-edge fields in recent years. Based on first-principles calculations, we systematically investigate the mechanical properties and electronic characteristics of transition metal oxyhalide TiOBr in this work. Results demonstrate that the TiOBr monolayer exhibits metallic characteristics with Dirac points located above the Fermi level. The calculated Fermi velocity of 0.32×10^6 m s^{-1} indicates its superior electron mobility. Furthermore, the TiOBr monolayer displays a negative Poisson's ratio (NPR) effect, establishing it as a promising candidate for auxetic materials. These distinctive properties endow the TiOBr monolayer with significant research value and application prospects in future nanoelectronics and mechanical functional materials.

Introduction

Two-dimensional (2D) materials have advanced rapidly in recent years.[1–3] Their superior properties compared to three-dimensional (3D) materials provide them with broad application prospects across diverse fields.[4–6] 2D materials, with structures ranging from monolayer to few-layer thickness, exhibit unique quantum confinement effects,[7,8] resulting in distinctive physical properties like the negative Poisson's ratio (NPR)[9] behavior. These auxetic materials expand laterally under longitudinal tension while contracting laterally under longitudinal compression, exhibiting the NPR effect.[10,11] Compared to materials with a positive Poisson's ratio (PPR), NPR materials exhibit enhanced mechanical properties, including high shear moduli, improved indentation resistance, greater fracture toughness and superior sound/vibration absorption.[12,13] Owing to these inherent advantages, NPR materials hold significant application prospects in fracture-resistant structures, energy storage systems and water desalination technologies.[14–16]

Although Gibson's theory initially predicted NPR behavior in 2D materials,[17] intrinsic NPR characteristics were not unambiguously confirmed until 2014 through combined experimental and theoretical studies on black phosphorus ($\nu = -0.027$).[18,19] This discovery stimulated widespread exploration of NPR phenomena in diverse low-dimensional materials, accelerating progress in nanoscale material design and property engineering. Subsequently, NPR has been confirmed in several 2D materials, broadly categorized into three groups: (1) out-of-plane NPR materials, such as BP_5 ($\nu = -0.037$),[20] black phosphorene ($\nu = -0.027$)[18] and borophene ($\nu = -0.053$);[21] (2) in-plane NPR materials, including penta-graphene ($\nu = -0.07$),[13] penta-B_2N_4 ($\nu = -0.02$),[22] MB_2 (M = Ti, Hf, V, Nb, Ta) ($\nu = -0.093$ to -0.337);[23] (3) bidirectional NPR materials, exemplified by $GaPS_4$ ($\nu_{\text{in-plane}} = -0.033$ and $\nu_{\text{out-of-plane}} = -0.62$)[24] and Ag_2S ($\nu_{\text{in-plane}} = -0.12$ and $\nu_{\text{out-of-plane}} = -0.52$).[25] Studies demonstrate that in most NPR materials, this effect stems primarily from intricate microstructural geometries, commonly through re-entrant or hinged mechanisms.[26] Emerging evidence also suggests a correlation between NPR and electronic structures, as observed in materials like WN_4 ($\nu = -0.103$)[27] and 1T-type MX_2 (M = Mo, W, Tc, Re; X = S, Se, Te) ($\nu = -0.03$ to -0.37).[28] These findings provide crucial theoretical foundations and research directions for the targeted discovery of novel NPR materials.

Moreover, the quantum confinement effect in 2D materials leads to novel electronic properties, such as the appearance of Dirac points near the Fermi level. Two-dimensional Dirac materials offer advantages including tunable carrier type, broad functional modulation flexibility and high electron mobility. Notably, specific materials such as MB_2 (M = Ti, Hf, V, Nb, Ta),[23] Sn_2BN[29] and $TiZrB_4$ (ref. 30) feature coexisting Dirac points and NPR. This unique combination enables them to simultaneously possess distinctive mechanical properties (*e.g.*, NPR) and tunable electronic characteristics (*e.g.*, carrier type). However, research on these materials remains limited, warranting further in-depth investigation.

In this study, we theoretically predicted a novel 2D monolayer: TiOBr, taken from the bulk TiOX (X = Cl, Br) crystal with space group *Pmmn* (no. 59)[31] with FeOCl structure type. The TiOBr monolayer possesses Dirac cone characteristics and NPR

---

[a] *School of Science, Shandong Jianzhu University, Jinan, Shandong, 250101, China. E-mail: yangbo19@sdjzu.edu.cn*

[b] *School of Science, Henan Agricultural University, Zhengzhou, Henan 450002, China*

† Authors contributed equally to this work.

behavior by using first-principles calculations based on Density Functional Theory (DFT). Molecular dynamics simulations and mechanical stability criteria confirm the dynamical stability at room temperature and mechanical stability of the TiOBr monolayer, respectively. TiOBr monolayer exhibits metallic characteristics. However, there have been Dirac points located above the Fermi level. The Fermi velocity of 0.32×10^6 m s^{-1} indicates its superior electron mobility. The corrugated TiOBr structure exhibits auxetic behavior, with a negative Poisson's ratio of $\nu_{xy} = -0.019$ and $\nu_{yx} = -0.008$. The in-plane Young's moduli (E_x and E_y) along the x- and y-directions are 100.59 and 42.76 GPa nm, respectively. The distinct values of negative Poisson's ratio and Young's modulus along the x- and y-directions demonstrate the mechanical anisotropy of TiOBr monolayer. TiOBr monolayer exhibits an ultimate tensile strain of 18%, demonstrating significant tensile resilience.

Method and computational details

Our first-principles calculations were carried out using the density functional theory (DFT) as implemented in the Vienna *ab initio* simulation package known as VASP.[32,33] The electron–ion interaction was described by projected-augmented-wave (PAW) potentials.[34] The generalized gradient approximation (GGA) in the form of the Perdew–Burke–Ernzerhof (PBE) was adopted for the exchange–correlation functional.[35] The Brillouin zone (BZ) integration was sampled on a grid of $15 \times 15 \times 1$ k-points according to the Monkhorst–Pack method for structural optimization. The energy cutoff employed for plane-wave expansion of the electron wave function was set to 600 eV. Structural optimizations were carried out using a conjugate gradient (CG) method until the remaining force on each atom was less than 0.01 eV Å^{-1}. Two-dimensional periodic boundary conditions were employed in the x–y plane, while a vacuum space up to 20 Å was applied along the z-direction to exclude the interaction between neighboring images.

Results and discussion

The geometric structure of the TiOBr layer with the $2 \times 2 \times 1$ supercell was shown in Fig. 1(a). The 2D TiOBr layer is a non-planar configuration with a bulking. The height of the bulking of TiOBr is 2.62 Å. The space group of TiOBr is *Pmm*2 (no. 25). The optimized lattice constants are $a = 3.44$ Å, $b = 3.35$ Å, respectively, which were obtained by minimizing the total energy. There are three atoms in one unit cell, containing one Ti atom, one O atom and one Br atom. From Fig. 1(b), we can see that one Ti atom is bonded with two Br atoms and two O atoms. The length of the Ti–Br bonds is 2.52 Å, the length of the Ti–O bonds is 1.86 Å, which is slightly shorter than the Ti–Br and Ti–O bonds in the bulk TiOBr (2.54 Å and 2.24 Å, respectively).[31] The shorter bond lengths in the 2D TiOBr layer indicate the strong chemical bond.

The stability of TiOBr monolayer

To investigate the thermal stability of this structure, we performed *ab initio* molecular dynamics simulations (AIMDS) on a large supercell containing 48 atoms within a Nose–Hoover thermostat at 300 K, 450 K and 600 K with a time step of 1.0 fs. After running 5000 steps, the geometry of TiOBr monolayer was well preserved without any structure collapse and the total energy of the system was converged in this time scale, as shown in Fig. 2(a)–(c). However, the TiOBr monolayer fails to retain its original geometric structure at 700 K. Therefore, the TiOBr monolayer exhibits good dynamic stability up to around 600 K. Compared to the bulk TiOBr crystal, the total energy of TiOBr monolayer is 0.31 eV per atom higher than that of bulk TiOBr crystal, which suggests its energetic disadvantage. Moreover, the phonon spectrum of the free-standing TiOBr monolayer has imaginary frequency modes. Without the support of a substrate, the freestanding TiOBr monolayer is likely unstable. To stabilize the TiOBr monolayer, we formed a heterostructure with TiOBr

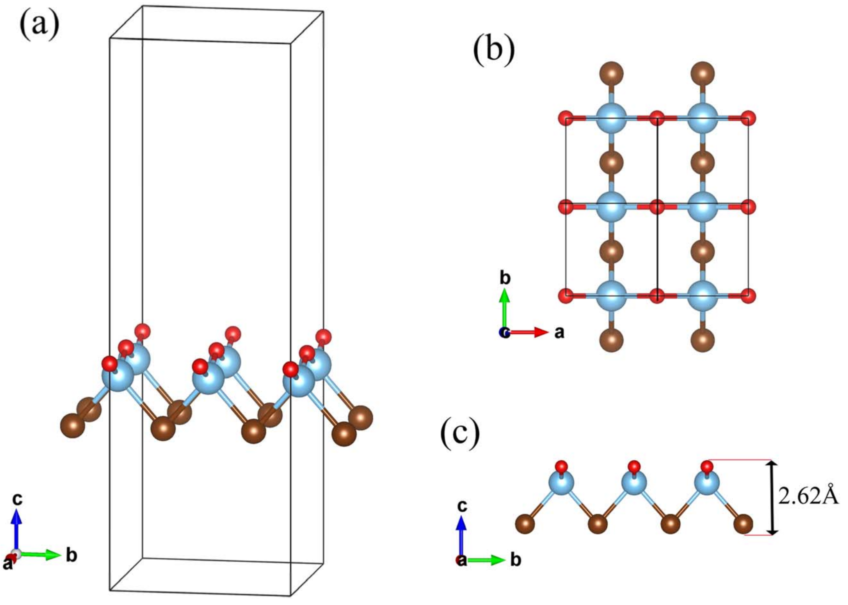

Fig. 1 (a) The geometric structure of TiOBr monolayer. (b and c) The top and the side view of TiOBr monolayer.

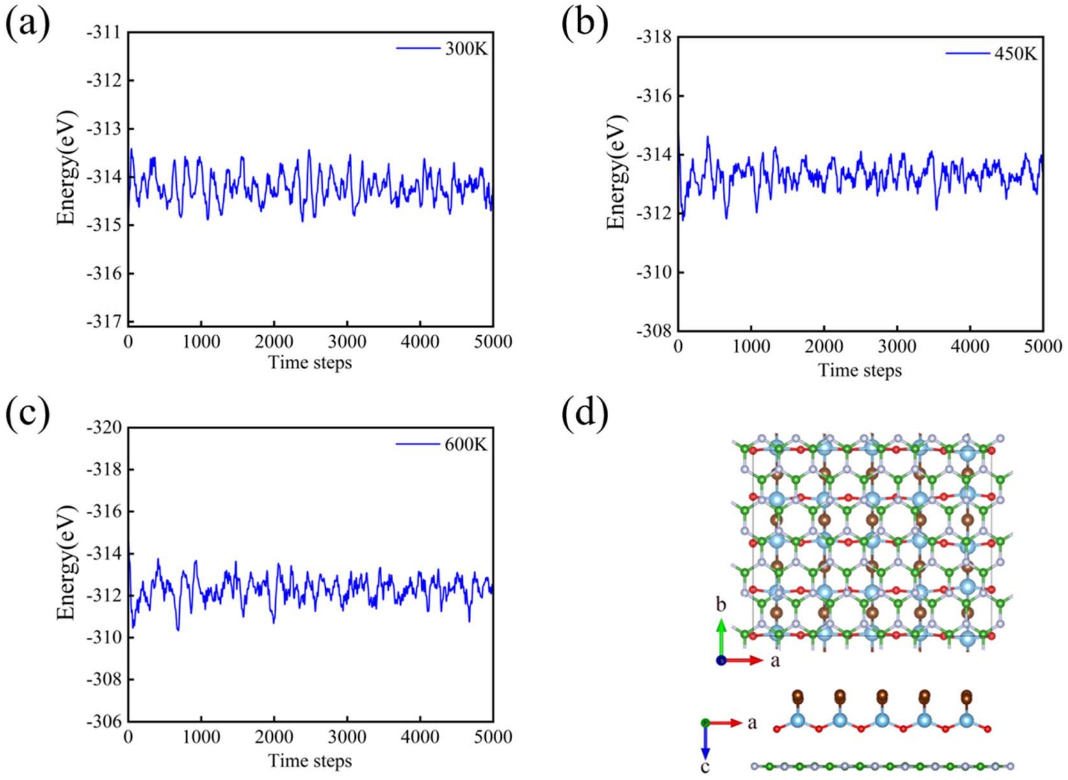

Fig. 2 The total energy fluctuations with respect to the simulation time at (a) 300 K, (b) 450 K and (c) 600 K. (d) The top and side view of atomic configuration of TiOBr/BN heterostructure, respectively.

and BN, as shown in Fig. 2(d). After optimization, the interlayer spacing is about 3.01 Å and the configuration of TiOBr monolayer in the BN–TiOBr heterostructure is well preserved, as shown in Fig. 2(d). We also compared the energy of the free-standing TiOBr monolayer and the TiOBr monolayer in heterostructure and found that the energy of TiOBr in heterostructure is lower than that of the free-standing TiOBr monolayer by 0.58 eV per atom, indicating that the van der Waals interaction between TiOBr and BN substrate reduces the energy of TiOBr, which showed that TiOBr monolayer is likely to exist stably on the BN substrate.

Electronic properties

The electronic band structure of TiOBr layer along the highly symmetric directions (M–Γ–K–M) in Brillouin zone is plotted in Fig. 3(a). From the calculated results, the TiOBr monolayer shows metal properties, with the Fermi level crossing the bands. However, there is a Dirac point above the Fermi level with two energy bands intersecting each other in the Γ–K direction. To better visualize the characteristics of these Dirac cones, we calculated their three-dimensional band structures, shown in Fig. 3(b). Notably, the Fermi velocity (ν_{F}) calculated by the formula $\nu_{\mathrm{F}} = \dfrac{\partial E}{\partial k}$ is 0.32×10^6 m s^{-1} along the Γ–K direction, which is one-third that of graphene (0.95×10^6 m s^{-1}).[36] Additionally, we calculated the orbital-resolved band structure projected onto different atomic orbitals, as shown in Fig. 3(c). The Dirac bands of TiOBr monolayer predominantly arise from the d-orbitals of Ti atoms, particularly the d_{xy} and d_{yz} orbitals, whereas the contributions from O atoms and Br atoms are almost negligible, confirming the dominant role of Ti d-orbitals in the formation of Dirac points. To further confirm the contribution of Dirac points to the electronic properties of TiOBr monolayer, we systematically calculated the isosurfaces of the Kohn–Sham wave functions in the vicinity of Dirac point, with the computational results presented in Fig. 3(d). These isosurfaces exhibit clear features of the d orbitals of the V atoms, in good agreement with the orbital-resolved band structure of TiOBr monolayer.

Mechanical properties

We verified the mechanical stability of TiOBr layer from the strain energy in response to in-plane lattice distortion. Using the standard Voigt notation, the elastic strain energy per unit area for 2D sheet can be expressed as:[13,37]

$$U = \frac{1}{2}C_{11}{\varepsilon_{xx}}^2 + C_{22}{\varepsilon_{yy}}^2 + C_{12}\varepsilon_{xx}\varepsilon_{yy} + 2C_{66}{\varepsilon_{xy}}^2$$

where ε_{xx} and ε_{yy} represent the uniaxial in-plane strains along the x- and y-directions, and ε_{xy} is the shear strain. The parameters C_{11}, C_{22}, C_{12} and C_{66} represent the components of the elastic modulus tensor, corresponding to the second partial derivation of strain energy with respect to strain. The elastic constants can be obtained by fitting the energy curves associated with uniaxial and equibiaxial strain, which are $C_{11} = 100.61$ GPa nm, $C_{22} = 42.77$ GPa nm, $C_{12} = -0.80$ GPa nm, $C_{66} =$

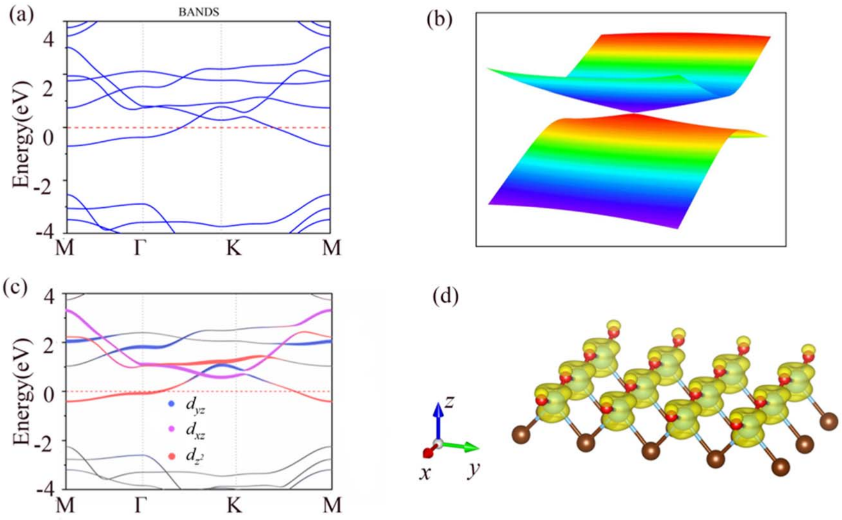

Fig. 3 (a) The electronic band structure of TiOBr with PBE functional. (b) The three-dimensional Dirac cone configuration of the Dirac point along Γ–K direction. (c) The orbital-resolved band structure of TiOBr monolayer projected onto different atomic orbital. The Fermi level was set to zero. (d) The charge density distribution in the vicinity of the Dirac point.

0.79 GPa nm, respectively. The elastic constants satisfy the criterion of the mechanical stability of 2D sheet: $C_{11} \times C_{22} - C_{12}^2 > 0$, $C_{66} > 0$, indicating that the TiOBr monolayer is mechanically stable. It is interesting to see the negative value of C_{12}, which gives rise to negative Poisson's ratios (NPR) of $\nu_{xy} = C_{12}/C_{22} = -0.019$, $\nu_{yx} = C_{21}/C_{11} = -0.008$. Poisson's ratio is an important mechanical index of materials, which measures the deformation of material in the orthogonal direction with respect to loading direction. Most materials have a PRR; that is, when stretching in one direction, the orthogonal direction is shortened. However, few materials exhibit NPR, known as auxetic materials. The auxetic materials can expand in the transverse direction when stretched. Such unusual mechanical behavior has been observed in 2D materials, such as Be_2C_5 monolayer ($\nu = -0.041$),[38] SiC_6 ($\nu = -0.042$),[39] $NiCl_2O_8$ ($\nu = -0.054$).[40]

For anisotropic graphical visualization, based on its elastic constants, Poisson's ratio $\nu(\theta)$ and Young's modulus $Y(\theta)$ as functions of the orientation angle ($0° \leq \theta \leq 360°$) can be calculated as follows, respectively:[41,42]

$$A = \frac{C_{11}C_{22} - C_{12}^2}{C_{66}} - 2C_{12}$$

$$B = C_{11} + C_{22} - \frac{C_{11}C_{22} - C_{12}^2}{C_{66}}$$

$$Y(\theta) = \frac{C_{11}C_{22} - C_{12}^2}{C_{22}\cos^4\theta + A\cos^2\theta\sin^2\theta + C_{11}\sin^4\theta}$$

$$\nu(\theta) = \frac{C_{12}\cos^4\theta - B\cos^2\theta\sin^2\theta + C_{12}\sin^4\theta}{C_{22}\cos^4\theta + A\cos^2\theta\sin^2\theta + C_{11}\sin^4\theta}$$

The TiOBr monolayer exhibits significant mechanical anisotropy, as shown in Fig. 4(a) and (b). Consequently, applying the same strain along different crystal orientations of the TiOBr monolayer induces distinct elastic responses. The direction-dependent in-plane Young's moduli (E_x and E_y) along the x- and y-directions are derived from the elastic constants using the formulas and are 100.59 and 42.76 GPa nm, which are much lower than the corresponding value for graphene[43] (340 N m^{-1}). Compared with graphene, TiOBr exhibits superior mechanical flexibility.

Furthermore, as expected, the TiOBr monolayer along both the x- and y-directions exhibits NPR mechanical behavior. The calculated results show that the Poisson's ratios of the TiOBr monolayer in the x- and y-directions are −0.019 and −0.008, respectively, consistent with previous calculations. This confirms that the TiOBr monolayer is indeed an auxetic material. This behavior primarily originates from minor distortions within its inherent $Ti_2O_2Br_2$ tetrahedral framework. Upon application of tensile strain along the x-axis, the t_2–p orbital coupling induces an increase in the ⟨Br–Ti–Br⟩ bond angle along the y-axis. This expansion along the y-axis consequently triggers the NPR effect in the TiOBr monolayer, as illustrated in Fig. 4(d). However, the observed NPR value is relatively small. This reduction is attributed to the weak t_2–p orbital coupling, demonstrated in Fig. 4(c).

To further confirm the NPR of TiOBr monolayer, we calculated the lateral strain in the y-direction when a tensile strain is applied along the x-direction and *vice versa*. We examined the cases with ε_x and ε_y equal to 1%, 3% and 5%. Clearly, the equilibrium lattice constant in the y-direction (x-direction) increased when subjected to tensile strain along the x-direction (y-direction), as shown in Fig. 5(a) and (b). However, when stretching in the x-direction, the stretching amount corresponding to the y-direction is bigger than the stretching amount in the x-direction when stretching in the y-direction in

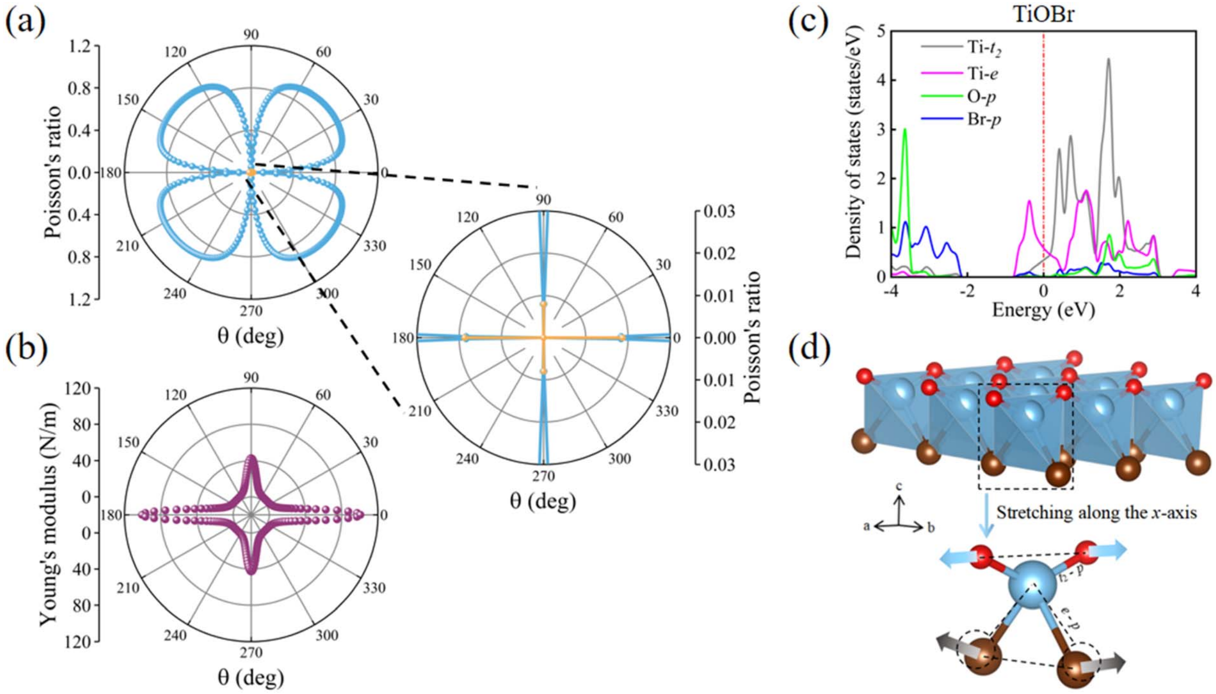

Fig. 4 Mechanical properties of monolayer TiOBr, (a) Poisson's ratio, (b) Young's modulus. The second column is an enlarged view of the NPR of the TiOBr monolayer. NPR and PPR are marked with yellow and blue lines, respectively. (c) Atom-projected density of states (DOS) of TiOBr. The DOS shown in the figure are t_2 (d_{xy}, d_{yz}, d_{zx}), e ($d_{x^2-y^2}$, d_{z^2}) and p (p_x, p_y, p_z). The Fermi level is set to zero. (d) The stress schematic illustrates the motion along the y-axis (gray arrow) in TiOBr under tensile strain applied along the x-axis (blue arrow).

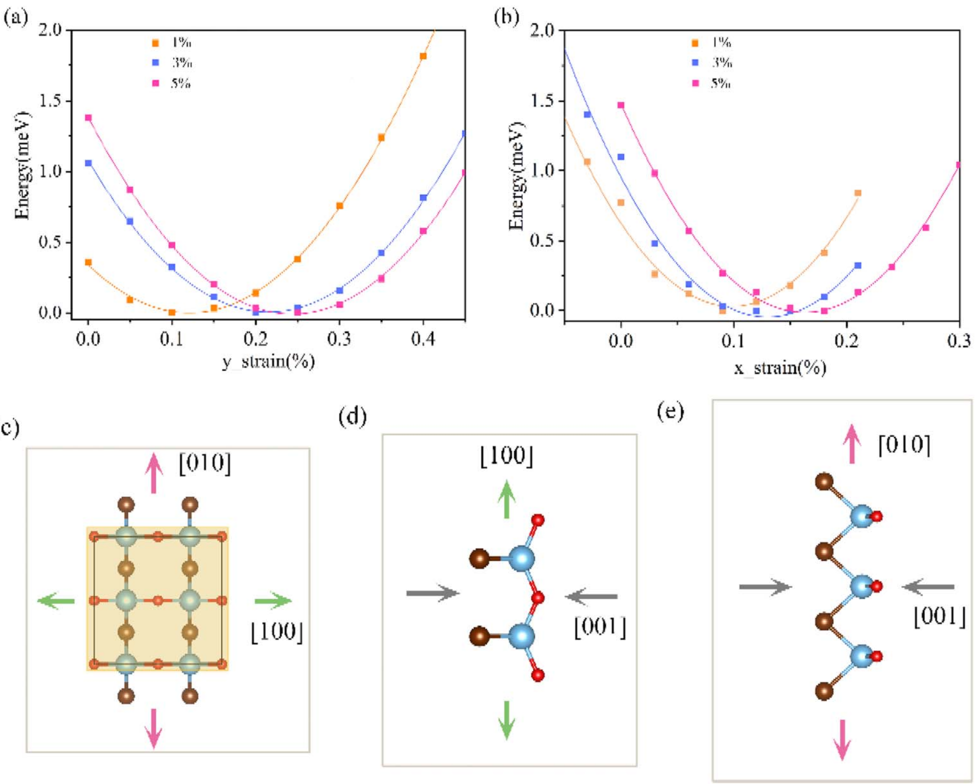

Fig. 5 (a and b) Strain energy with respect to the lateral lattice response when the TiOBr lattice is under strain along the x- and y-directions. (c–e) Three orthographic views of the TiOBr unit responsible for NPR along the [001], [010] and [100] directions. The expansion and compression along the [100], [010] and [001] directions are indicated by the green, pink and grey arrows, respectively.

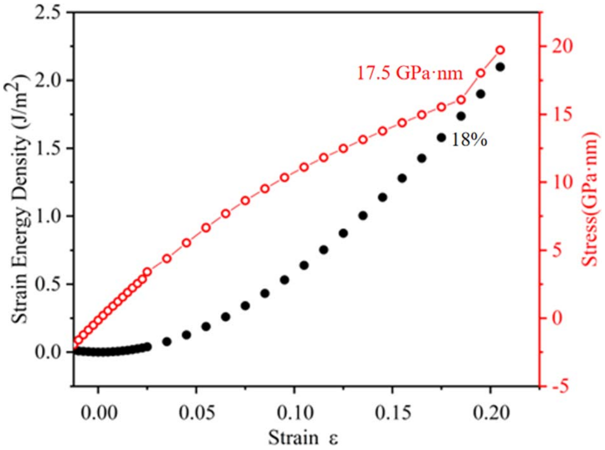

Fig. 6 The strain energy density of TiOBr under the uniform strain and the stress–strain responses.

the same stretching scale. That is consistent with the Poisson's ratio given previously.

The anisotropic Poisson's ratios are closely related to the unique bulking framework and the low-dimensional effect. A schematic representation of the origins of NPR is plotted in Fig. 5. When a small longitudinal expansion occurs along the green row, the height of the bulking is reduced (as indicated by the grey arrows), making the lateral lattice dilate and *vice versa*. Conversely, if a small lateral stretch occurs along the pink row, it will cause longitudinal expansion in the same way. The TiOBr exhibits direction-dependent Poisson's ratios. This mechanism offers a strategy for the design of auxetic materials.

We next determine the maximum strain tolerance of TiOBr monolayer by applying the uniform biaxial strain: $\varepsilon = (a_\varepsilon - a_0)/a_0$, a_ε represents the strained lattice parameter in the post-deformation configuration, a_0 represents the unstrained lattice parameter of the undeformed configuration. The strained structures were optimized at a series of lattice parameters with an increment of 2%. The strain energy density: $E_{sd} = (E_\varepsilon - E_0)/S_0$ profile as a function of biaxial strain, as shown in Fig. 6, which can be expanded as a function of strain in a Taylor series incorporating quadratic and higher-order terms. The quadratic components characterize linear elastic deformations, while higher-order terms account for nonlinear elastic deformation and strain evolution. Through the derivative of strain energy with respect to strain, we derived the corresponding stress–strain relationship, which is co-plotted in Fig. 6, which shows the ultimate strain is 18% and the corresponding ultimate stress is about 17.5 GPa nm. This suggests that the TiOBr monolayer exhibits a relatively high resistance to stretching.

Conclusions

We employed first-principles calculations based on density functional theory (DFT). The results indicate that the TiOBr monolayer exhibits metallic behavior. Notably, a Dirac point is present above the Fermi level, with a Fermi velocity of 0.32 × 10^6 m s^{-1}. Molecular dynamics simulations confirm the structural stability of the TiOBr monolayer at 300 K. Concurrently, criteria for mechanical stability also attest to its mechanical stability. It is particularly noteworthy that the mechanical properties of the TiOBr monolayer display pronounced anisotropy: its Young's modulus is 100.59 and 42.76 GPa nm along the *x*- and *y*-directions, which exhibits superior mechanical flexibility. Similarly, its negative Poisson's ratio also exhibits anisotropy, with values of −0.019 and −0.008 along the *x*- and *y*-directions, respectively, indicating the mechanical anisotropy of TiOBr monolayer. Our theoretical calculations predict a metallic TiOBr monolayer exhibiting NPR behavior, demonstrating superior mechanical and electronic properties and possessing the potential to be an ideal candidate material for future electronic devices and magneto-mechanical systems.

Conflicts of interest

There are no conflicts to declare.

Data availability

Data underlying the results presented in this paper may be obtained from the authors upon reasonable request.

Acknowledgements

This work was supported by the National Natural Science Foundation of China (no. 12104258).

References

1 Y. D. Ma, Y. Dai, M. Guo and B. B. Huang, *Phys. Rev. B: Condens. Matter Mater. Phys.*, 2012, **85**, 235448.
2 Y. Liang, J. W. Li, H. Jin, B. B. Huang and Y. Dai, *J. Phys. Chem. Lett.*, 2018, **9**, 2797–2802.
3 C. X. Huang, J. Zhou, H. P. Wu, K. M. Deng, P. Jena and E. J. Kan, *Phys. Rev. B*, 2017, **95**, 045113.
4 P. Zhou, C. Q. Sun and L. Z. Sun, *Nano Lett.*, 2016, **16**, 6325–6330.
5 Y. L. Feng, X. M. Wu, J. C. Han and G. Y. Gao, *J. Mater. Chem. C*, 2018, **6**, 4087–4094.
6 N. H. Miao, B. Xu, L. G. Zhu, J. Zhou and Z. M. Sun, *J. Am. Chem. Soc.*, 2018, **140**, 2417–2420.
7 P. Miró, M. Audiffred and T. Heine, *Chem. Soc. Rev.*, 2014, **43**, 6537–6554.
8 Z. B. Gao, X. Dong, N. B. Li and J. Ren, *Nano Lett.*, 2017, **17**, 772–777.
9 R. Peng, Y. D. Ma, Q. Wu, B. B. Huang and Y. Dai, *Nanoscale*, 2019, **11**, 11413–11428.
10 R. Lakes, *Adv. Mater.*, 1993, 293–296.
11 X. K. Ma, J. Liu, Y. C. Fan, W. F. Li, J. F. Hu and M. W. Zhao, *Nanoscale Adv.*, 2021, **3**, 4554–4560.
12 C. W. Huang and L. Chen, *Adv. Mater.*, 2016, **28**, 8079–8096.
13 S. H. Zhang, J. Zhou, Q. Wang, X. S. Chen, Y. Kawazoe and P. Jena, *Proc. Natl. Acad. Sci. U. S. A.*, 2015, **112**, 2372–2377.

14 C. S. Liu, H. H. Zhu, X. J. Ye and X. H. Yan, *Nanoscale*, 2017, **9**, 5854–5858.
15 C. Si, W. H. Duan, Z. Liu and F. Liu, *Phys. Rev. Lett.*, 2012, **109**, 226802.
16 S. Babaee, J. Shim, J. C. Weaver, E. R. Chen, N. Patel and K. Bertoldi, *Adv. Mater.*, 2013, **25**, 5044–5049.
17 L. J. Gibson and M. F. Ashby, *Proc. R. Soc. London, Ser. A*, 1982, **382**, 43–59.
18 Y. C. Du, J. Maassen, W. R. Wu, Z. Luo, X. F. Xu and P. D. Ye, *Nano Lett.*, 2016, **16**, 6701–6708.
19 J. W. Jiang and H. S. Park, *Nat. Commun.*, 2014, **5**, 4727.
20 H. D. Wang, X. X. Li, J. Y. Sun, Z. Liu and J. L. Yang, *2D Mater.*, 2017, **4**, 045020.
21 L. Z. Kou, Y. D. Ma, C. Tang, Z. Q. Sun, A. J. Du and C. F. Chen, *Nano Lett.*, 2016, **16**, 7910–7914.
22 M. Yagmurcukardes, H. Sahin, J. Kang, E. Torun, F. M. Peeters and R. T. Senger, *J. Appl. Phys.*, 2015, **118**, 104303.
23 C. M. Zhang, T. W. He, K. Matta, T. Liao, L. Z. Kou, Z. F. Chen and A. J. Du, *J. Phys. Chem. Lett.*, 2019, **10**, 2567–2573.
24 J. H. Yuan, K. H. Xue, J. F. Wang and X. S. Miao, *J. Phys. Chem. Lett.*, 2019, **10**, 4455–4462.
25 R. Peng, Y. D. Ma, Z. L. He, B. B. Huang, L. Z. Kou and Y. Dai, *Nano Lett.*, 2019, **19**, 1227–1233.
26 W. Z. Xiao, G. Xiao, Q. Y. Rong and L. L. Wang, *Phys. Chem. Chem. Phys.*, 2018, **20**, 22027–22037.
27 W. Y. Jin, W. G. Sun, X. Y. Kuang, C. Lu and L. Z. Kou, *J. Phys. Chem. Lett.*, 2020, **11**, 9643–9648.
28 L. P. Yu, Q. M. Yan and A. Ruzsinszky, *Nat. Commun.*, 2017, **8**, 15224.
29 K. Y. Shi, D. D. Zhao, S. S. Li, W. X. Ji, C. W. Zhang and P. J. Wang, *ACS Appl. Electron. Mater.*, 2024, **6**, 174–182.
30 S. Pramchu, P. Srisakonsub, S. Sucharitakul, A. P. Jaroenjittichai and Y. Laosiritaworn, *Comput. Condens. Matter*, 2022, **31**, e00679.
31 H. G. V. Schnering, M. Collin and M. Hassheider, *Z. Anorg. Allg. Chem.*, 1972, **387**, 137–141.
32 K. E. Evans and A. Alderson, *Adv. Mater.*, 2000, **12**, 617–628.
33 Y. Li, S. D. Luo, M. C. Yang, R. Liang and C. C. Zeng, *Adv. Funct. Mater.*, 2016, **26**, 2900–2908.
34 B. Anasori, M. R. Lukatskaya and Y. Gogotsi, *Nat. Rev. Mater.*, 2017, **2**, 16098.
35 A. J. Mannix, X. F. Zhou, B. Kiraly, J. D. Wood, D. Alducin, B. D. Myers, X. L. Liu, B. L. Fisher, U. Santiago, J. R. Guest, M. J. Yacaman, A. Ponce, A. R. Oganov, M. C. Hersam and N. P. Guisinger, *Science*, 2015, **350**, 1513–1516.
36 S. Woo, H. C. Park and Y. W. Son, *Phys. Rev. B*, 2016, **93**, 075420.
37 R. C. Andrew, R. E. Mapasha, A. M. Ukpong and N. Chetty, *Phys. Rev. B: Condens. Matter Mater. Phys.*, 2012, **85**, 125428.
38 Y. Wang, F. Li, Y. F. Li and Z. F. Chen, *Nat. Commun.*, 2016, **7**, 11488.
39 X. B. Liu, X. F. Shao, B. Yang and M. W. Zhao, *Nanoscale*, 2018, **10**, 2108–2114.
40 H. B. Zhao, H. G. Wang, W. Tan, N. Ren, L. H. Ding, X. Yu and A. Z. Wang, *Phys. Chem. Chem. Phys.*, 2023, **25**, 31050–31056.
41 M. Born, K. Huang and M. Lax, *Am. J. Phys.*, 1955, **23**, 474.
42 Y. Yoo, J. H. Yang and J. H. Lee, *Curr. Appl. Phys.*, 2018, **18**, 799–802.
43 C. Lee, X. D. Wei, J. W. Kysar and J. Hone, *Science*, 2008, **321**, 385–388.